

Hubble Space Telescope times-series photometry of the planetary transit of HD189733: no moon, no rings, starspots

Frédéric Pont¹, Ronald L. Gilliland², Claire Moutou⁶, François Bouchy³, Timothy M. Brown⁴, David Charbonneau⁵, Michel Mayor¹, Didier Queloz¹, Nuno Santos⁷, Stéphane Udry¹

¹Geneva University Observatory, 1290-Sauverny, Switzerland

²Space Telescope Science Institute, 3800 San Martin Drive, Baltimore MD 21128, USA

³Laboratoire d'Astrophysique de Paris, 98bis Bd Arago, 75014 Paris, France

⁴Las Cumbres Observatory, Goleta CA 93117, USA

⁵Smithsonian Center for Astrophysics, 60 Garden Street, Cambridge MA 02138, USA

⁶Laboratoire d'Astrophysique de Marseille, Travers du Siphon, 13376 Marseille Cedex 12, France

⁷Centro de Astrofísica da Universidade do Porto, Rua das Estrelas, 4150-762 Porto, Portugal

Received date / accepted date

Abstract. We monitored three transits of the giant gas planet around the nearby K dwarf HD 189733 with the ACS camera on the Hubble Space Telescope. The resulting very-high accuracy lightcurve (signal-to-noise ratio near 15000 on individual measurements, 35000 on 10-minute averages) allows a direct geometric measurement of the orbital inclination, radius ratio and scale of the system: $i = 85.68 \pm 0.04$, $R_{pl}/R_* = 0.1572 \pm 0.0004$, $a/R_* = 8.92 \pm 0.09$. We derive improved values for the stellar and planetary radius, $R_* = 0.755 \pm 0.011 R_\odot$, $R_{pl} = 1.154 \pm 0.017 R_J$, and the transit ephemerides, $T_{tr} = 2453931.12048 \pm 0.00002 + n \cdot 2.218581 \pm 0.000002$. The HST data also reveal clear evidence of the planet occulting spots on the surface of the star. At least one large spot complex (> 80000 km) is required to explain the observed flux residuals and their colour evolution. This feature is compatible in amplitude and phase with the variability observed simultaneously from the ground. No evidence for satellites or rings around HD 189733b are seen in the HST lightcurve. This allows us to exclude with a high probability the presence of Earth-sized moons and Saturn-type debris rings around this planet. The timing of the three transits sampled is stable to the level of a few seconds, excluding a massive second planet in outer 2:1 resonance.

Key words. planetary systems – stars: individual: HD 189733 – techniques: photometric

1. Introduction

The star HD 189733 is transited by a close planetary companion (Bouchy et al. 2005). The brightness of the host star ($V=7.7$ mag), the short period (2.2 days) and the large planet-to-star radius ratio ($R_{pl}/R_* \approx 0.15$) make it the most favourable system known for detailed studies. In the year following the discovery of its transiting planet, HD 189733 has already been subjected to many follow-up observations, including extensive ground-based transit photometry (Bakos et al. 2006, Winn et al. 2007), measurement of the spin-orbit angle using the Rossiter-McLaughlin effect (Winn et al. 2006), and measurement of the infrared flux distribution of the planet with the secondary eclipse (Deming et al. 2006, Grillmair et al. 2007).

A precise knowledge of the radius of the planet is essential to all applications. From the transit lightcurve, one can measure the geometry of the system, hence the orbital angle, the size of the star and the size of the planet. However, to first order the orbital angle and the stellar radius can compensate almost

perfectly. Ordinary ground-based lightcurves do not reach the accuracy required to lift the degeneracy between orbital angle and stellar radius, because of systematics induced by the atmosphere. The mass and radius of the star need to be fixed with model-dependent assumptions. From space, lightcurves of sufficient accuracy to lift the orbital angle vs. primary radius degeneracy can be obtained, as spectacularly illustrated with the HST/STIS lightcurve of HD 209458 by Brown et al. (2001).

In this article we present extreme-accuracy photometry of the transit of HD 189733 with the ACS camera on the Hubble Space Telescope. Acquiring such photometry has two justifications: (1) to obtain a direct, "geometrical" measurement of the size of the host star, (2) to detect possible Earth-size satellite or Saturn-type debris rings around the planet HD 189733b.

2. Observations

We have observed HD 189733 with the Hubble Space Telescope during 3 visits of 5 orbits each, using the ACS/HRC and the grism G800L (program GO-10923). In this configura-

tion, the first-order spectrum range from 5500 Å to 10500 Å with ~ 40 Å per pixel. The first visit occurred on May 22, 2006 (JD 245877.718 to 878.092), the second on May 26 (882.115 – 882.408) and the third on July 14 (930.946 – 931.240).

To achieve the highest possible S/N, we observed with relatively long exposures (25s), allowing the ACS detector to saturate by a factor about 5 at the wavelengths near 700 nm where it is most sensitive. Prior experience doing time-series photometry with the ACS show that with proper analysis, Poisson-limited photometry can be obtained even with images that are much more saturated than this. This is done by integrating over enough pixels to capture essentially all electrons generated by the stellar photons, even though they may have diffused away from the pixel where they were created. For crowded field photometry, this approach can be problematic because of leakage from adjacent star images, but for spectroscopy on the bright HD189733 this is not a problem.

We obtained extremely high S/N spectrophotometry in a time-series mode with a cadence of about 60s. Since the transit duration is more than the length of an HST orbit and the target star can be seen for less than half of each orbit, three visits were required to obtain full phase coverage of the transit. We accumulated a total of 675 exposures for the three visits. Each visit contains two full orbit before the transit, two that are all or partly inside the transit, and one that falls entirely after the transit. Observations on both sides of the transits are necessary for each visit so that clear out-of-transit baselines can be established. Also, the first HST orbit often exhibits unique systematics as the telescope and instrument stabilize at the new pointing. The first orbit of each visit is not utilized in the final time series analyses.

3. Reductions

Our analysis started with the images provided by the STScI pipeline. These are corrected for overscan and bias image subtraction, dark reference file subtraction after scaling to individual exposure times, and corrected from digital units to electrons scaling by the detector gain. Retrievals from the STScI archive were made only after final biases and darks were available.

These images are not flat-fielded for grism data. For the very similar GO/DD-10441 observations of TrES-1 in which HRC grism spectra at high S/N were obtained at nearly the same place on the detector, but without the complication of saturation and bleeding, it was found that use of a wavelength dependent flat field provided no benefit. Facing the extra complication here of saturated data and needing to take into account the flat fields as a function only of electron origination, not current location, we simply have not applied flat fields for these data. For our purposes of deriving differential time series over time, in which all of the spectra have been taken at nominally the same pointing, and for which the extractions are averaged over a large domain (over 5000 pixels for the global first order spectrum extraction), we would not expect much sensitivity to flat fielding errors. If there were no motion of the spectra relative to the detector as a result of HST guiding errors, there should be no need to flat field. These guiding errors, while not zero, are quite small, and at a later step we decorrelate with

vectors that remove any small noise resulting from lack of flat fielding.

3.1. Extraction

The images consist of a direct image, a first-order spectrum, and a partial second-order spectrum, inclined diagonally across the detector. The signal of saturated pixels is spread along columns (i.e. in the y direction). Analyses start with measurement of x, y position for the single direct image taken at the start of each visit. The calibration given in ACS-ISR 03-07 is used to provide a wavelength for each position along the spectrum trace. The global first-order spectrum extraction involves a sum over 173 columns that span wavelengths of about 5370 to 10690 Å. The extractions involve sums over columns, rather than attempting extractions in the pure cross-dispersion direction. For non-saturated data this results in a moderate loss of spectral resolution, for saturated data the resolution loss is inherent in the data anyhow. We define an arbitrary data value at which to extend the summations to along columns, stopping the summation the first time the data drop below this value. A number of trials are run adopting a range of these arbitrary sum limiting values, and the one providing highest S/N (after applying all the corrections discussed later) is adopted. For HD 189733 a stopping value of 6,000 electrons works best (peak intensities would have been over 10^6 in the absence of saturation, thus the sums extend to levels of less than 1% relative intensity.) A first extraction is done using the above procedure, and intensities are normalized by the mean for all points (except first) in orbits two and five – this provides an initial light curve. We perform a cosmic ray elimination step by sigma clipping data values outside the saturated data region (with a buffer of two pixels), over the full stack of images in each visit – after normalizing out the intensity variations during transit via use of the preliminary light curve. After replacing data values affected by cosmic rays the normalization is reset. The sigma clipping is done after providing a model for the intensity variations based on a linear regression with the six external variables to be described below in the decorrelation section. Cosmic ray elimination is not very important for this project that used short exposure times and accumulated over 5×10^8 source electrons each exposure. The latter procedure could only catch cosmic rays outside the saturated pixel domain. To search for cosmic rays within the saturated pixel region we formed stacks of column-summed intensities, and performed the same data modelling and sigma clipping step as above. This resulted in trivial improvements for 2 of 3 visits, and a minor loss for the third. We have kept this step although it neither helped nor harmed the overall result to any significant extent.

For a specific application (see Section 4.5), we also extracted sub-sections of the spectrum in two wavelength intervals, restricting the extraction to specific ranges in y .

3.2. Decorrelation

It is important to establish by how much the spectrum moves relative to the detector exposure-to-exposure, and at the same

time establish records of other characteristics such as measures of the cross-dispersion width and the rotation of the spectrum relative to the detector. Such external vectors become candidates for performing decorrelations with the intensity vectors.

For each time step a one-dimensional Gaussian was fit to all columns in the first- and second-order spectra for which (a) the core does not saturate, (b) the column is not next to one that saturates, and (c) the column intensity sum reaches 10^5 electrons. The results of these fits are then averaged together. After subtracting the mean this provides time series records of: (1) mean y -position of the spectra, (2) a measure of the spectrum width – Gaussian sigma, and (3) a rotation formed by differencing mean y -position in first and last 10 columns which for these data are separated by about 65 columns. A measure of the spectrum shifts in x are derived by forming a one-dimensional vector of column-summed intensities over x , averaged over all the exposures in a visit. Pixel-by-pixel in x the intensity derivative in x is formed, and note is taken of the region (columns 2-15 in practice) that has both decent signal and strong derivatives. Then averaged over these 14 columns the relative intensities in individual spectra in combination with the dI/dx derivative provide delta- x shifts for each exposure. The spectrum shifts in x with a characteristic pattern each orbit by about 0.1 pixel peak to peak. A somewhat larger offset occurs in y , with both a long-term drift and within orbit variations present. The cross-dispersion width becomes more variable with each successive orbit. Rotation maintains a characteristic pattern each orbit. The lowest panel is just a common linear position of data within each orbit (to account for other effects related to the orbital phase of HST).

Decorrelations are performed by evaluating a multi-linear regression on these vectors simultaneously: x -position, y -position, width, rotation, orbit phase, and overall time. No attempt is made to account for the fact that several of these external vectors show mutual correlations. The regression is based on a least squares fit using all of the points outside of transit, ignoring orbit 1. Then the full set of data points is divided by the fit to provide corrections for noise that correlate with these external vectors.

No additional sigma-clipping of the data has been performed. Exposure 65 of visit 02 is affected by a strong cosmic ray and was not used.

3.3. Systematics after decorrelation

Since a primary objective of this program is to measure deviations from the transit shape at the level of a fraction of a millimagnitude, it is crucial to estimate the level of systematics that could remain in the data after decorrelation. One method is to use decorrelation trials in which some out-of-transit orbits are not used in the regression to establish the decorrelation. Here there are two visits, the first (V1) and second (V2) that have two orbits either after (V1) or before (V2) the transit. The exercise is to step through not using either orbits 2 or 3 of V2, or orbits 4 or 5 of V1. The residuals are then compared to those in which all of the data were used. The results were very clear. In the 4 orbits (total) not used in decorrelations the largest de-

viations remained under 10^{-4} , with means typically an order of magnitude smaller still. In no case did any residual show deviations similar in magnitude to those seen multiple times for orbits inside the transits.

A second method, this time to check if some real signal could have been removed by the decorrelation, is to insert features in the data before decorrelation, and check how they are recovered. Decorrelation trials in which signals similar to those in V2 (rise from 0.0 to +0.5 mmag in about 10 points followed by a drop back to 0.0 in 10 points) are added to the time series before decorrelation. We chose to add these to either orbits 2 or 3 of V2, or 4 or 5 of V1 (one at a time). In 4 of 6 total cases this triangle-shaped perturbation was added to centers of orbits, in the other 2 it was added near the end of orbits. In each case the signal is preserved through the decorrelation step at the 80-90% level. It is not surprising that there is a slight reduction in height resulting from having added in a positive signal.

The above two tests show that: (a) the out-of-transit orbits stay less noisy, and show no systematics even when not used to establish the decorrelation, and (b) if real systematic deviations had been present that last only a fraction ($\sim 1/3$ rd) of an orbit, these would only be affected at the 10-20% level by decorrelation. This adds significantly to believing the residual features seen during the in-transit HST orbits are real, and likely reflect flux inhomogeneities on the surface of the star.

We also tested that our results are not sensitive to the size of the extraction box used, by repeating the analysis with a limit at 2,000 electrons (instead of 6,000).

3.4. Absolute flux

Previous experience with ACS and HST show that the variability of ACS over a few weeks is about 0.003 to 0.004. Much of the deviation is correlated with known variation of focus. After correcting for these variations, an epoch-to-epoch precision of $\sim < 0.002$ can be obtained.

The visit-to-visit changes of total intensity are, based on the mean of orbits 2 and 5 without the first point in orbits: +0.005 for visit V2 relative to visit V1, and +0.007 for V3 relative to V1. The Poisson limit on these would be less than $5 \cdot 10^{-6}$. There is a large caveat that needs to apply to V3 – this is after the switch to Side 2 electronics in early July 2006. There could be a minor change in operating temperature. We don't expect a change, but there is a potential zero-point difference for visit V3.

4. Results

4.1. Lightcurve

The lightcurve decorrelated from dependence on instrumental parameters is given in Table 1, and shown in Figure 1. The data in the first orbit of each visit, not used in the analysis, are not shown.

The standard deviation of the individual data points outside the transit is 67×10^{-6} . Expressed in terms of signal-to-noise, this corresponds to 15000:1. The photon noise is 45×10^{-6} .

Date	Flux
2453877.71866	0.999421
2453877.71935	0.999318
2453877.72005	0.999580
2453877.72074	0.999518
2453877.72143	0.999498
2453877.72213	0.999603
2453877.72282	0.999592
2453877.72352	0.999637
2453877.72421	0.999532
2453877.72491	0.999610

Table 1. Photometric time series (electronic table)

The standard deviation on 10-points average is 28×10^{-6} , corresponding to a S/N of 35000:1.

No out-of-transit structure is visible in our lightcurve above the level of the residual instrumental systematics.

Transit lightcurves are expected to be perfectly symmetrical to better than the 10^{-4} level. Two asymmetric features are apparent in our data during the transit, one at the end of the second orbit of the first visit, the other at the beginning of the third orbit of the second visit. We label the first "Feature A" in our analysis, and the second "Feature B".

Feature A is much too large to be explained by an instrumental effect, and no special behaviour of the telescope was observed at the corresponding time. The flux increase during Feature A is also seen in the zeroth-order image on the CCD. It is accompanied by a detectable change of spectral distribution, which suggests an explanation in terms of the transiting planet occulting a cool spot on the surface of the star (see Section 4.5).

Feature B is also larger than instrumental effects, and does not correlate with any of our external instrumental parameters. Its less regular shape and the fact that any colour effect is below the noise level indicate that, in principle, an explanation in terms of instrumental noise cannot be entirely excluded. Based on our experience with previous HST high-accuracy times series, and the simulations of Section 3.3, we believe, however, that Feature B is also real.

We do not use Features A and B in the analysis of the lightcurve in terms of planetary transit. They are treated separately in Section 4.5.

4.2. Stellar activity and variability

HD 189733 is an active star, variable to the percent level. It is listed in the Variable Star Catalogue as V452 Vul. A chromospheric activity index of $S = 0.525$ has been measured by Wright et al. (2004). Activity-related X-ray emissivity has been measured by both EXOSAT and ROSAT, activity-related radial velocity residuals of 15 m s^{-1} were reported by Bouchy et al. (2005). Winn et al. (2007) have measured the photometry variability of this star extensively and confirm variability at the percent level, compatible with an explanation in terms of transit spots modulated by a rotation period of $P_{rot} \sim 13.4$ days. Moutou et al. (2007) measure strong activity in the CaII line and time-varying magnetic field signatures. The explanation of

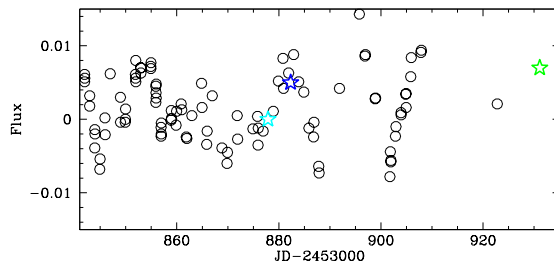


Fig. 2. Photometry of HD 189733 from Winn et al. (2007; *dots*), with the timing and mean flux level of the three HST visit indicated (shifted by an arbitrary constant; *stars*).

Features A and B in terms of starspots is therefore natural. The presence of large starspots is also confirmed by an observing campaign on this object by the MOST satellite (E. Miller-Ricci et al., in prep.).

The Winn et al. (2007) photometry is contemporaneous with our HST data. Our absolute measurements are placed within the context of the ground-based monitoring in Fig. 2, with an arbitrary zero-point shift. The HST data is in agreement with the periodic variation seen in the long-term lightcurve. If we interpret this variability in terms of starspots moving in and out of view with the rotation of the star, then the third visit occurs near the brightest point – with less star spots visible – and the first visit with a 0.007 dimming due to starspots. The phasing and amplitude of features A and B are perfectly compatible with an explanation in terms of the planet occulting part of the starspots responsible for the photometric variation (see Section 4.5).

Before fitting a transit signal, we correct for the variations of the total stellar luminosity due to the presence of starspots. Outside of features A and B, the planet crosses a spot-free region, therefore a region slightly brighter than the average over the stellar disc, which includes the spots. This is a tiny correction of the scaling between transit depth and radius ratio (of the order of 2×10^{-4} in flux). Nevertheless, to the level of the accuracy of the HST lightcurve, it makes a significant difference and must be accounted for. We use the absolute flux differences measured in Section 3.4.

4.3. Transit signal

A transit light curve computed with the Mandel & Agol (2002) algorithm was fitted to the light curve, with a downhill simplex algorithm (Press et al. 1992). Features A and B were removed with cuts from JD=877.875 to the end of orbit 3 of visit 1, and from the beginning of orbit 3 of visit 2 to JD=882.333. The limb-darkening coefficients were left as free parameters, using the four-coefficients non-linear expression of Claret (2000). They converge to $a_{1-4} = (0.506, -0.727, 1.345, -0.519)$. These values are compatible with the ones for $T_{eff} = 5000\text{K}$, $[\text{Fe}/\text{H}]=0.0$ and $\log g = 4.5$ for the R filter.

The resulting best-fit transit parameters are shown in Table 2. The best-fit theoretical transit curve and the residuals are shown in Fig. 1.

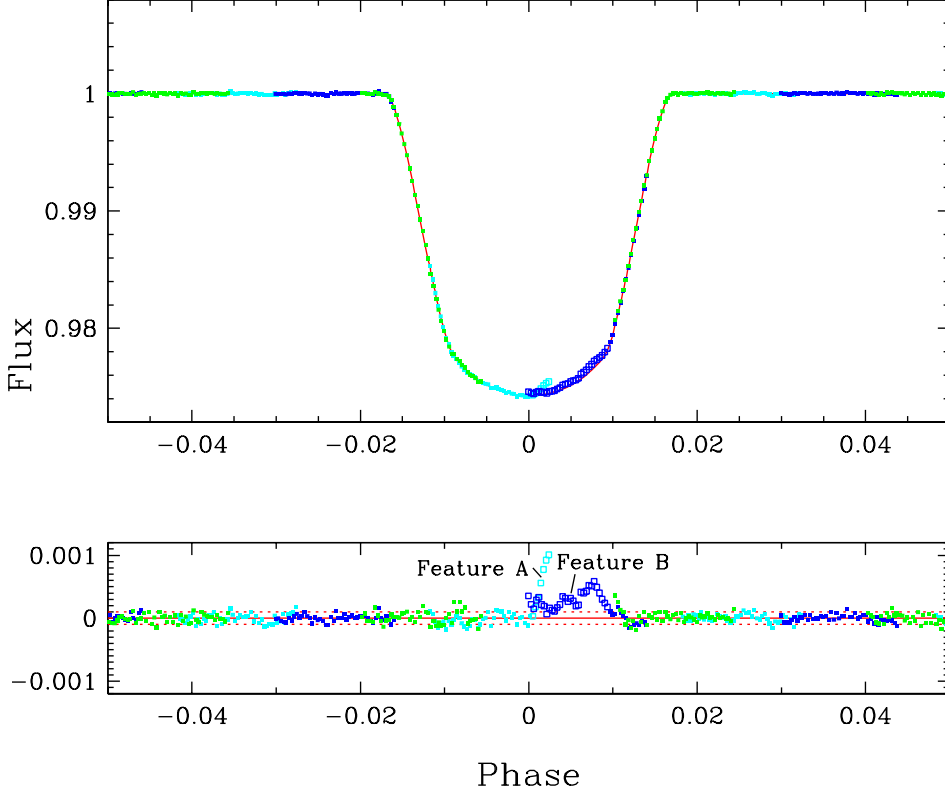


Fig. 1. Decorrelated lightcurve phased to $P=2.218583$ days, with best-fit model transit curve. **Top:** flux after external parameter decorrelation as a function of phase; **Bottom:** residuals around the best-fit transit model. Light blue for the first visit, dark blue for the second and green for the third. Open symbols indicate data affected by Features A and B (see text), not used in the fit.

<i>Measured in this paper</i>	
Period	2.218581 ± 0.000002
Transit epoch	$2453931.12048 \pm 0.00002$
Radius ratio R_{pl}/R_*	0.1572 ± 0.0004
System scale a/R_*	8.92 ± 0.09
Impact parameter	0.671 ± 0.008
Orbital angle	85.68 ± 0.04
Host star $M^{1/3}/R$ ratio	1.242 ± 0.012
Visit 1 transit epoch	$2453877.87448 \pm 0.00005$
Visit 2 transit epoch	$2453882.31171 \pm 0.00005$
Visit 3 transit epoch	$2453931.12048 \pm 0.00003$
<i>Inferred</i>	
Stellar radius [R_\odot]	0.755 ± 0.011
Planetary radius [R_J]	1.154 ± 0.017
<i>Adopted</i>	
Stellar mass [M_\odot]	0.825 ± 0.025
Planetary mass [M_J]	1.15 ± 0.04

Table 2. Parameters of the transiting system HD 189733.

photon noise, and is due to the presence of systematic fluctuations on the scale of 10^{-4} , even outside Features A and B. These fluctuations may be due to systematics not perfectly corrected by the decorrelation, or to structures on the surface of the star smaller in scale than those responsible for Features A and B (see Section 4.5).

Including parts or all of Features A and B in the fit, or changing the limb darkening coefficients within reasonable limits, does not modify the resulting system parameters beyond the 1% level, and therefore has no influence on the astrophysical applications.

The photon-noise uncertainties on the transit parameters are extremely small, and the actual uncertainties are dominated by correlated flux residuals. The amplitude of the residuals and the tests in Section 3, show that these effects are of the order of 10^{-4} at most over the relevant timescales. We therefore estimate the uncertainties on the transit parameters by allowing the data to move, as a whole, by a maximum of 10^{-4} in flux from the model, following the approach of Pont, Zucker and Queloz (2006) to derive error intervals in the presence of correlated noise. These values can be considered upper limits for the uncertainties, since the systematics are unlikely to be exactly in

The standard deviation of the residuals around the model lightcurve in the transit are 129×10^{-6} . This is larger than the

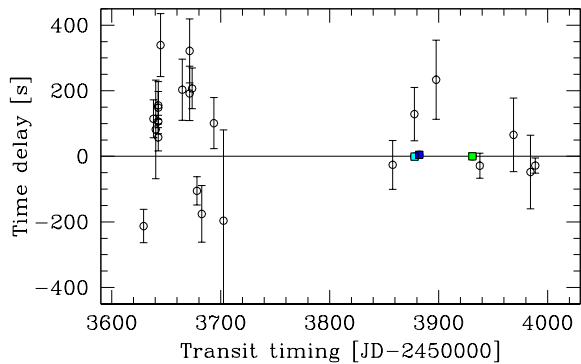


Fig. 3. Transit timing residuals for HD 189733, from Bakos et al. (2006), Winn et al. (2007) and this paper, relative to our best-fit ephemerides. The three HST transits are indicated by the larger squares.

phase with the differences caused by changing the transit parameters.

The uncertainties due to these fluctuations, in turn, are dominated in the derivation of the physical parameters of the system by the uncertainty on the stellar mass and radius, due to the $RM^{-1/3}$ degeneracy of transit systems. As an order-of-magnitude indication, the photon noise uncertainty on the radius ratio is $\sim 0.01\%$, the uncertainty due to systematics is $\sim 0.1\%$, and the uncertainty due to $RM^{-1/3}$ degeneracy is $\sim 1\%$ (See Section 4.6).

4.4. Transit timings

Table 2 also gives the values of the epoch of the three transits covered by our HST data, when fitted independently with the other parameters fixed at the values given by the combined data.

We compared these values with previous ground-based measurements (see Figure 3). The HST transit timing are compatible with previous determinations, while being much more precise. The periodicity of the transits is stable at the level of a few seconds over the three HST transits. This strongly suggests that the χ^2 excess seen in the transit timing for ground-based data is due to unrecognised systematics, as suggested by Bakos et al. (2006), rather than real orbital variations.

Deviations of transit timings from strict periodicity can reveal the existence of other planets in the system (e.g. Agol et al. 2005). However, the relation between transit timing variations and the orbital elements of the unseen perturber is very complex, and non-detections exclude only restricted regions of parameter space. In our case, periodicity at the level of a few seconds excludes, for instance, the presence of an Earth-mass body in 2:1 resonance with the giant planet (see figure 5 of Agol et al. 2005).

4.5. Moons, rings, and spots

No evidence is seen in the flux residuals for the characteristic signature of: (a) a transiting satellite or second planet (b)

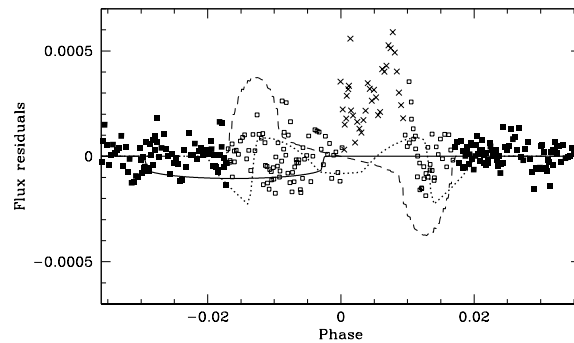


Fig. 4. Residuals around the best-fit transit model. Open symbols indicate data during the transit, crosses data attributed to Features A and B. The lines show the signals expected from an additional transiting 0.8 Earth-radius body (solid), from planetary rings (dotted), and from transit timing variations of 20 seconds (dashed).

planetary rings (c) planet or star oblateness (d) transit timing variations. The residuals around the best-fit transit lightcurve are compared to the expected shapes for three effects in Fig. 4.

The two asymmetrical features observed during the transits do not have the correct shape to be explained in terms of the transit of a second body in the system. They do not occur at the phase expected for such effects as the presence of rings, non-sphericity of the star or planet. Feature A and B are best explained as due to the passage of the planet in front of cooler regions – starspots, spot complexes or plages – on the surface of the star itself.

Feature A, to first order a linear rise in flux, can be well explained by the planet occulting part of a large cooler region on the star. Feature B is less regular and has lower S/N. Its exact shape is sensitive to uncertainties on the limb darkening parameters and the absolute flux difference between the HST visits.

For the duration of Feature A, the planet moves $\sim 80\,000$ km across the face of the star. The orbital and rotation axis of the system are almost aligned (Winn et al. 2006) and the rotation velocity of the star is long compared to the duration of the transit (Winn et al. 2007), so that this distance corresponds to a similar projected distance in longitude on the surface of the star. This gives the minimal extension in longitude of the spot responsible for Feature A.

The minimum latitude extension of the spot is given by the total flux increase of Feature A. If the spot is much cooler than the rest of the star surface, the flux it emits is negligible, and it can be considered a dark feature. In that case, the width needed to produce the observed flux increase is 12 000 km. At the other extreme, the occulted portion of the spot cannot be larger than the diameter of the planet, $R \sim 165\,000$ km. To produce the observed drop in flux, a spot of this size will need to have a temperature less than 100 K degrees cooler than the rest of the star.

Both solutions produce fits to the data that are within the colour uncertainties.

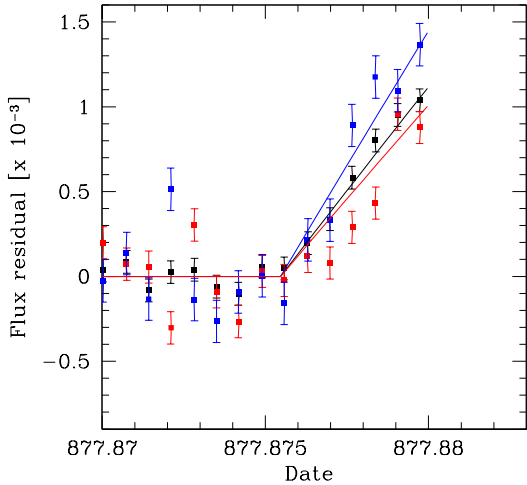


Fig. 5. Evolution of the “white” (dots), “blue” (5500-6500 Å; circles) and “red” (8500 - 10500 Å; triangles) flux before and during Feature A. The lines show the effect of a spot 12000 km wide and 1000 K cooler than the stellar effective temperature.

There is one additional constraint in the data to support the spot scenario. The occultation of a starspot is expected to be significantly “blue”, in the sense that as a cooler and redder region is occulted, the spectrum will become bluer. The magnitude of the effect will depend on the effective temperature of the spot compared to the rest of the star. To first order though, in the passbands that we use and for the temperature of HD 189733, a cool and a warmer spot will produce similar colour signatures, because the temperature difference will be compensated by the size of the spot so as to produce an effect of similar amplitude in the total light curve.

We computed the flux in our spectra from 5500 to 6500 Å, and from 8500 to 10500 Å (approximate wavelength limits, see Section 3), thus defining a “blue” and a “red” passband. Figure 5 shows the evolution of the flux in these passbands during Feature A and during an equal interval of time just before, on the same HST orbit. The colour effect is clearly visible, and in the expected direction. We computed the colour change expected for starspots of different vertical (latitude) extension and temperature difference, using the constraint of the total flux change from the “white” lightcurve. An example is shown in Figure 5. We use the blackbody approximation for the spectrum of the star and spot. This simplification is justified given the amplitude of the effects compared to the observation uncertainties.

In summary, Feature A is compatible with a complex of cool spots extending at least 80 000 km in longitude and 12 000 km in latitude, in a relatively uniform manner, with an overall effective temperature much lower than the rest of the star. It is also compatible with a larger, more circular spot, with a smaller temperature difference, down to about $\Delta T < \sim 100$ K for a spot as wide or wider than the planet.

The same procedure was repeated for Feature B. However, in this case, the total amplitude of the effect is too small, and any colour signature is dominated by the uncertainties. Also, the more complex shape of the signal is compatible with several arrangements of spots. Therefore, while we posit that the flux variations corresponding to Feature B are due to the occultations of activity-related features on the surface of the star, we do not attempt to model this feature in detail. In the limit of large temperature difference (dark spots), the size of the spots responsible for Feature B would have to be equivalent to a circle of 9 000 km radius (more than one spot would be necessary to reproduce the observed lightcurve shape).

4.6. Host star and planet

The radius of the primary and its mass to the one-third power are degenerate in transit lightcurves. Second-order effects that would allow breaking this degeneracy, such as the light travel-time effect, are far too small to be detectable in the presence of any realistic amount of photometric noise or stellar variability. Therefore, the $M^{-1/3} R$ degeneracy must be lifted with recourse to stellar evolution models.

Fortunately, HD 189733 is a well-observed, low-mass star, and evolution models allow for only a small range of masses compatible with its observed visible and infrared magnitude, parallax, and spectroscopic temperature. Its Hipparcos parallax of 51.94 ± 0.87 mas implies a distance of 19.25 ± 0.32 parsec, and absolute magnitudes of $M_V = 6.25$ in the visible and $M_K = 4.07$ in the infrared. These luminosities can be combined with the $M^{-1/3} R = 1.246 \pm 0.012$ (in Solar units) value from the HST transit shape and confronted to stellar evolution models. Figure 7 shows the error box for HD189733 in these two projections of parameter space compared to the position of Padova stellar evolution models (Girardi et al. 2002). The data is coherent with the models and compatible with a mass in the 0.80-0.85 M_\odot range for HD 189733. Similar results are obtained using the Baraffe et al. (1998) low-mass star models. We therefore confirm the value of $M = 0.825 \pm 0.025 M_\odot$ used in Bouchy et al. (2005) for the mass of the host star.

It is interesting to note that low-mass eclipsing binaries with well-determined mass and radius do not lie on the model tracks in this range of mass (Ribas et al. 2006), unlike HD 189733. This is a strong indication confirming the suspicion that close eclipsing binaries strongly influence each other, and are therefore not good calibrators for the mass-radius relation of single stars.

We adopt $M = 0.825 \pm 0.025 M_\odot$ to lift the mass-radius degeneracy, which implies $R_{star} = 0.753 \pm 0.011 R_\odot$, and $R_{pl} = 1.147 \pm 0.017 R_J$ (with $R_J = 71500$ km). These values are listed in Table 2.

The planetary mass remains unchanged at $M_{pl} = 1.15 \pm 0.04$ from Bouchy et al. (2005). This corresponds to a planetary density of 822 kg m^{-3} .

5. Discussion

The ACS spectrophotometric time series presented in this article shows the capacity of HST to obtain lightcurves of ex-

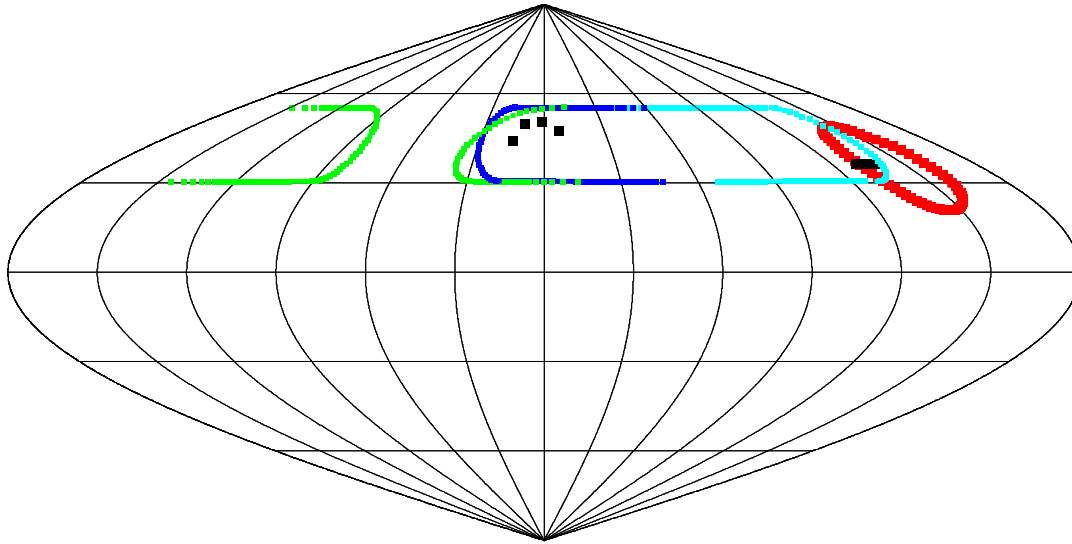


Fig. 6. Map of the surface of HD 189733, showing the geometrical configuration of HST visits and the spots needed to explain Feature A and B on a map of the star’s surface (equi-area projection, lines every 30 degrees). The projection of the planet edge’s path in front of the star is shown in light blue for the first visit, dark blue for the second, and green for the third. Sparser symbols indicate a high angle between the stellar surface and the line-of-sight. The minimum ($T < 4000$ K) and maximum ($T > 4900$ K) spot models are shown for Feature A in black and red respectively, and some arbitrary symbols for small spots for Feature B. The impact parameter between the spots and planet is arbitrary. The star rotates in the Eastward direction with an assumed period of 11.8 days.

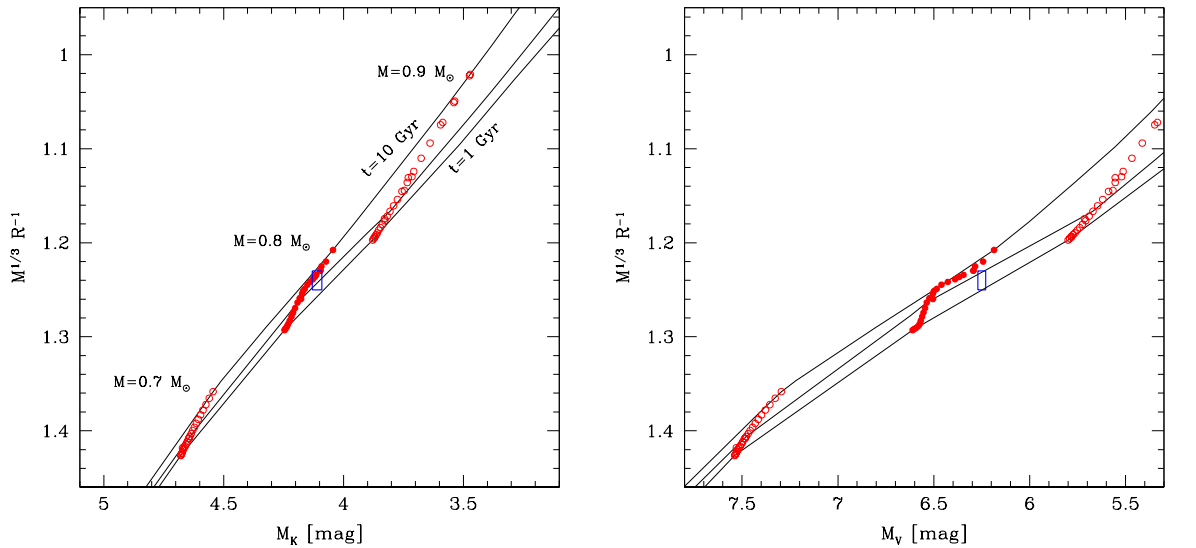


Fig. 7. Constraints on HD 189733 from the absolute visible and infrared magnitude, and the $M^{1/3} R^{-1}$ ratio, compared to Padova stellar evolution model isochrones.

treme accuracy for bright stars. It echoes the HST lightcurve of Brown et al. (2001) acquired with the STIS spectrograph for HD 209458. The S/N for HD 189733 is even higher because of the larger wavelength domain covered (at lower spectral resolution), and the fact that HD 189733 is slightly brighter in the wavelength interval sampled, and the higher throughput of ACS/HRC.

The single-point standard deviation outside the transit is 67×10^{-6} , for a sampling of one point per minute. Correlated systematics left after decorrelation of instrumental parameters such as tracking drift and focus change have an amplitude well below the 10^{-4} level. The standard deviation of the mean of measurements over 10 minutes is 28×10^{-6} . By comparison, systematics in high-precision ground-based photom-

etry are typically of the order of one part per thousand, or 1000×10^{-6} .

These data allow a very precise measurement of the planetary radius to be obtained. This is also due to the fact that the constraints on the mass of the stars are good, because it is a low-mass star with a known parallax from Hipparcos.

The HST/ACS lightcurves permit to lift the degeneracy between primary radius and inclination angle in the transit signal. Bakos et al. (2006) show how the data of a ground-based photometric campaign, even with several telescopes and in several filters, can lead to misleading conclusions in this respect. The Bakos et al. data apparently indicated a much smaller primary ($R_* = 0.68 \pm 0.02 R_\odot$), but the authors concluded that this was due to unrecognized systematics in the ground-based photometry. We reinforce this conclusion. Our results, on the other hand, confirm the values of Winn et al. (2007), with smaller uncertainties. We conclude that Winn et al. shows the proper amount of data necessary to lift the radius-inclination degeneracy from the ground with confidence, for such a deep transit: 8 complete transits covered in excellent conditions. This gives a yardstick against which to evaluate similar ground-based campaigns.

More recently, Baines et al. (2007) have measured the radius of HD 189733 directly with the CHARA interferometer, obtaining $R_* = 0.779 \pm 0.052 R_\odot$. This value has higher uncertainties but is completely independent of any assumption of mass, and is therefore a useful check to the determinations from the geometry of the transit. It is compatible with our value.

We here quantify our non-detection of moons or rings in terms of upper limits to any satellite or ring system around HD 189733b.

We have an upper limit of 10^{-4} to the depth of any unrecognised second eclipse in our data. This corresponds, given the size of the primary star, to a body of 5000 km (0.8 Earth radii). Unless the satellite spends each of the three transits that we have sampled either in front or behind the planet – an extremely unlikely configuration – we conclude that a moon larger than $0.8 R_\oplus$ around HD 189733b is excluded by the data. Figure 4 shows the signal such a moon would cause, superimposed to the residuals during the three HST visit.

We also exclude a ring system that would cause a flux drop larger than 10^{-4} around the time of transit. Since the planet is orbiting very close to the star and is subject to strong tides, we assume that any ring system would be aligned with the orbital plane ($i = 85.72$). In that case, a Saturn-type ring system at about $1 R_{pl}$ from the star’s surface will need to be less than 120τ km wide, where τ is its optical depth (if Saturn’s ring are any guide, a ring system should be thin enough that the ring’s thickness be negligible compared to its inclination even for the low inclination of HD 189733, so that this result is valid for any viewing angle of the rings except exactly edge-on). For comparison, the Saturn main ring system is 40 000 km wide with a high optical depth (~ 0.3), and the Jupiter ring system is also thousands of km wide but has a very small optical depth (10^{-6} to 10^{-7}). We can therefore exclude a major debris ring around HD 189733b (discounting the unlikely coincidence of an exact alignment with the line-of-sight).

We note that altogether these limits would not have allowed us to detect any of Jupiter’s moons, and Jupiter’s weak ring sys-

tem. Therefore, the absence of moon and rings in HD 189733 shown by our data must be understood as showing the absence of major, Earth-size moons and Saturn-type debris rings.

The fact that spot-like features affected a large part of the HST transits suggests that activity-related features are abundant on the surface of HD189733. The three HST visits together occulted slightly less than 10% of the star’s surface, revealing one spot at the 10^{-3} level and one at the $4 \cdot 10^{-4}$ level. This is in good order-of-magnitude agreement with the variability observed by Winn et al. (2007), which changes from negligible to 1% over a few rotation cycles.

A coherent picture of the active surface of HD189733 emerges from the combination of the small-scale information from HST data and the large-scale variability monitored by Winn et al. (2007). The timing of the sudden flux rise seen at the end of the first HST visit (“Feature A”) is compatible with the planet occulting part of a large spot responsible for a significant fraction of the modulation of the lightcurve. Between the first and the second visit, the luminosity of the star has increased by 0.5%, and about a quarter-period has elapsed, giving the spot (or spots) enough time to rotate from slightly east of the center of the star to the hidden side. Thus a high-latitude spot with a size comparable to that of the planet would explain all observations.

Fig. 6 shows the projection of the planet on the surface of the star during the three HST visit, and possible configurations for the observed features on the surface, assuming a rotation period of 11.8 days (refined period from the continuous monitoring of HD 189733 with the MOST satellite, E. Miller-Ricci, priv. comm). Incidentally, the Figure shows that the steeply increasing residuals at egress in the third visit may be due to crossing Feature B again.

Another possible explanation should be mentioned for Features A and B. Since both features occur when the planet occults the sub-planetary point on the star, rather than spots that rotate with the star, we may be seeing active regions on the star triggered by the star-planet interaction. Features A and B would then be a “footprint” of the planet on the sub-planetary point. Such features are expected from magnetic reconnections in magnetic interactions of the stellar corona with the planet magnetosphere. Such interaction could trigger chromospheric heating and flare-like activity, as predicted by Cuntz et al (2000) and simulated by Ip et al. (2004). From the combined analysis of the HST lightcurve and the monitoring of the stellar magnetic field performed by CFHT/ESPADoNs a couple of rotation cycles apart (Moutou et al. 2007), it could be possible to extrapolate the magnetic field topology and test or constrain such a scenario. More high quality photometric data would also be required to confirm the putative stability of relative positions between the planet and the active region of flux tube’s reconnection.

In conclusion, our results demonstrate again the potential of HST to gather extremely precise lightcurves for bright stars. We derive improved new measurements of the characteristics of this important systems, that provide very tight constrains for the models. Our lightcurve did not show any evidence for Earth-like satellites or rings around the planet HD 189733, nor transit timing variations indicative of an unseen second planet.

The lightcurve during the transit was strongly affected by the spots and active regions crossed by the planet, providing a rare glimpse of the small-scale geometry of spots on a star other than the Sun.

Bibliography

- Agol, E.; Steffen, J.; Sari, R.; Clarkson, W. 2005, MNRAS 359, 567
- Baines, E. K. ; van Belle, G. T. ; ten Brummelaar, T. A. ; McAlister, H. A. ; Swain, M.; Turner, N. H. ; Sturmann, L. ; Sturmann J 2007, ApJ Letters 661, 195
- Bakos, G. .; Knutson, H.; Pont, F.; Moutou, C.; Charbonneau, D.; Shporer, A.; Bouchy, F.; Everett, M et al. 2006, ApJ 650, 1160
- Baraffe, I.; Chabrier, G.; Allard, F.; Hauschildt, P. H. 1998, A& A 337, 403
- Brown, T. M.; Charbonneau, D.; Gilliland, R. L.; Noyes, R. W.; Burrows, A. 2001, ApJ 552, 699
- Claret, A. 2000, A& A 363, 1081
- Cuntz, M.; Saar, S.H.; and Musielak Z.E. 2000, ApJ 533, L151
- Deming, D.; Harrington, J.; Seager, S.; Richardson, L. J. 2006, ApJ 644, 560
- Girardi, L.; Bertelli, G.; Bressan, A.; Chiosi, C.; Groenewegen, M. A. T.; Marigo, P.; Salasnich, B.; Weiss, A. 2002, A& A 391, 195
- Grillmair, C. J.; Charbonneau, D.; Burrows, A.; Armus, L.; Stauffer, J.; Meadows, V.; Van Cleve, J.; Levine, D. 2007, ApJ 658, 115
- Ip, W.H.; Kopp, A.; and Hu J.H. 2004, ApJ 602, L53
- Mandel, K.; Agol, E. 2002, ApJ 580, 171
- Moutou, C.; Donati, J.-F.; Savalle R. et al. 2007, A&A in press
- Pont, F.; Zucker, S.; Queloz, D. 2006, MNRAS 373, 231
- Press, W.H.; Teukolsky, S.A.; Vetterling, W.T. 1992, "Numerical recipes in FORTRAN", Cambridge University Press
- Ribas, I. 2006, Ap & SS 304, 89
- Winn, J. N.; Johnson, J. A.; Marcy, G. W.; Butler, R. P.; Vogt, S. S.; Henry, G. W.; Roussanova, A. et al. 2006, ApJ 653, 69
- Winn, J. N.; Holman, M. J.; Henry, G. W.; Roussanova, A.; Enya, K.; Yoshii, Y.; Shporer, A.; Mazeh, T. et al. 2007, AJ 133, 1828
- Wright, J. T.; Marcy, G. W.; Butler, R. Paul; Vogt, S. S. 2004, ApJS 152, 261